Turkish Journal of Physics

http://journals.tubitak.gov.tr/physics/

Research Article

Turk J Phys
(2018) 42: 1 – 12

doi:10.3906/fiz-1704-27

Annealing effect of gold thin films on the light output performances of organic light emitting diodes

Selin PIRAVADILI MUCUR*, **Emine TEKİN**
The Scientific and Technological Research Council of Turkey (TÜBİTAK)
Marmara Research Center (MAM), Materials Institute, Kocaeli, Turkey

Received: 25.04.2017 • **Accepted/Published Online:** 13.10.2017 • **Final Version:** 13.02.2018

Abstract: Gold thin films (GTFs) are transferred onto a nanostructured surface and their effects on the characteristics of organic light emitting diodes (OLED) are investigated. GTF deposition is realized by the physical vapor deposition technique under high vacuum. Globose gold nanostructures are successfully generated by annealing GTFs at different temperatures. Atomic force microscopy reveals morphological changes affected by film thicknesses and annealing temperatures. In the tailored device architecture, GTFs, [poly(3,4-ethylenedioxythiophene):poly (styrenesulfonate) and poly[2-methoxy-5-(2-ethylhexyloxy)-1,4-phenylene vinylene are used as a hole injection layer, a hole transport layer, and an emissive layer, respectively. The performances of the fabricated OLEDs are enhanced in the presence of gold nanostructures obtained by thermal annealing GTFs coated onto the anode electrode of the devices. GTF thickness of 4.0 nm and an annealing temperature of 500 °C yield a nearly 2.6 times increase in the light output of the OLEDs.

Key words: Gold thin film, gold nanostructures, OLED, electroluminescence, thermal annealing

1. Introduction

Development and improvement of optoelectronic devices mainly depends on the materials used in the fabrication of the devices. π-Conjugated electroluminescent polymers have been widely used as charge recombination and transporting layers of organic light emitting diodes (OLEDs), organic photovoltaics (OPVs), and organic field effect transistors [1–4]. These materials are beneficial for organic electronics due to their tunable luminescence colors and ability to form thin films via the solution process. Therefore, studies aiming to improve performances of π-conjugated polymers are important for industrial and academic applications.

Recently, the application of nanoparticles (NPs) has been a prevailing research topic in order to enhance the performances of polymer OLEDs [5–9]. Due to their small dimensions ($<$100 nm), nanostructures have high surface/volume ratio and high surface energy compared to bulk materials. Moreover, the size-dependent physical and chemical properties of NPs differ greatly from their single atoms or molecules and bulk materials due to quantum confinement effects. This has given rise to enormous potential for applications of NP-based technologies in medical, biological [10], sensor [11], and electronic fields [12]. Semiconductor [13], polymeric [14], and, most commonly, metal NPs [15] have been investigated. Application of NP–polymer blends to OLEDs is encouraging, since NPs enhance device current efficiency and lifetime due to surface plasmon resonance (SPR) [16]. There are various studies about SPR used in optoelectronics, such as molecular sensing [17], OPVs [18,19],

*Correspondence: selin.piravadili@tubitak.gov.tr

electrochromic devices [20,21], and light-emitting diodes [22–24]. SPR is usually dependent on NP size and geometry, the dielectric properties of the metal, and the dielectric properties of the matrix where the NPs are embedded [25,26]. When metal NPs are located near the emissive layer, metal-enhanced fluorescence occurs due to the plasmon resonance with the incident light. Among the metal NPs, gold NPs have attracted much attention due to their distinct properties, such as large optical enhancements resulting in the strong scattering and absorption of light [27–29].

In a study by Xiao et al., an increase in electroluminescence (EL) intensity was obtained through the resonance between radiation and localized SPR around gold NPs [30]. Furthermore, in the work by Kumar et al., an ultrathin gold layer consisting of gold nanoclusters was incorporated as an interlayer between the electron-transport layer and the electrode of the OLED. This ultrathin gold layer improved the efficiency of OLEDs [31]. A thin film of gold was used in extensive applications such as micro- and nano-sized electromechanical systems, bioengineering, sensors and electronic textiles, generating nonlinear optical properties, and enhanced Raman scattering [32–34].

Deposition of multilayers in a controlled manner is crucial for the fabrication of micro- and optoelectronic devices. In the work by Sun et al., a thin film of gold was coated on graphene substrates via thermal evaporation; afterwards, gold NPs with different shapes were created using thermal annealing [35]. Hardy investigated the optical properties of gold thin films (GTFs) with different thicknesses that had been annealed at various temperatures [36]. As a result, a correlation was found between SPR absorbance and film thicknesses. Ung et al. analyzed the optical properties of Au@SiO2 particle films as a function of the particle volume fraction, using the Maxwell–Garnett model [37]. Schaub et al. investigated the different surface properties of thermally annealed gold nanostructures. It was found that thermal annealing led to the creation of large bulge structures in the gold layer [38]. Gouvêa et al. obtained NPs by annealing a GTF deposited on glass substrates [39]. Morphological and optical linear/nonlinear properties were investigated, before and after annealing, as a function of the film thickness. In the work by Ahamad, thin films were deposited using the Langmuir–Blodgett technique and atomic force microscopy (AFM) topographic images of the silver nanocube monolayer were recorded at different annealing times [40]. Ahn et al. transformed the ultrathin electroluminescent film coated on the fused quartz surface to NPs via annealing at 250 °C [41]. Islands of gold film were observed using successive thermal treatments.

There are different methods for creating NPs, such as inert-gas condensation and chemical synthesis [6,9,42]. Inert-gas condensation is frequently used to generate NPs from bulk metals with low melting points. In a vacuum chamber, vaporized metal is super-cooled with an inert gas stream. The super-cooled metal vapor condenses into nanometer-sized particles, which can be dragged with the inert gas stream and deposited onto a substrate. Chemical synthesis (sol-gel processing) is a wet chemical synthesis process used to generate nanostructures by gelation, precipitation, and hydrothermal treatment [43]. Thermal annealing is much faster, easier and more nontoxic than any other method, including inert-gas condensation.

In our contribution, influences of gold nanostructures on polymer OLED characteristics were investigated for the first time. GTFs were evaporated on glass substrates to obtain nanostructures through the thermal annealing. Afterwards, these nanostructures were used in an OLED architecture and device performances were measured. For the OLED application, GTF evaporation was carried out on indium tin oxide (ITO) substrates. Poly(3,4-ethylenedioxythiophene):poly (styrenesulfonate); (PEDOT:PSS)], [Poly[2-methoxy-5-(2-ethylhexyloxy)-1,4-phenylene vinylene]; (MEH-PPV), and 2,2',2'-(1,3,5-benzenetriyl) tris-[1-phenyl-1H-benzimidazole] (TPBi) were used as a hole transport layer (HTL), an emissive layer, and an electron transport

layer (ETL), respectively. Impacts of the nanostructured GTF on the device performances such as turn-on voltage, luminance, and current efficiency were studied systematically.

2. Materials and methods

The ITO-coated glass substrates (ITO thickness 120 nm, 15 ohms/sq.) were purchased from Visiontek Systems Ltd (East Dundee, IL, USA). Aluminum (Al), calcium (Ca), and gold pellets (99.99% pure) were purchased from Kurt J. Lesker Company (Jefferson Hills, PA, USA). PEDOT: PSS and MEH-PPV (Mn approximately 40,000–70,000) were purchased from Heraeus Clevios GmbH (Hanau, Germany) and Sigma-Aldrich (St. Louis, MO, USA), respectively. PEDOT:PSS was filtered through a 0.45 μm membrane PVDF filter. The MEH-PPV solution was prepared in toluene:1.2-dichlorobenzene (V:V, 3:1) mixture with 8 mg/cm^3 concentration. It was filtered through a 0.45 μm PTFE membrane filter. Patterned ITO-coated glass substrates were cleaned ultrasonically in an acetone detergent solution (PCC-54 2% wt dispersed in H_2O) and then cleaned with deionized water and isopropyl alcohol, in turn. Except HTL, all device layers were deposited in a glove-box system.

Hamamatsu PMA-12 C10027 Photonic Multichannel analyzer and digital multimeter (2427-C 3A; Keithley, Cleveland, OH, USA) were used to measure EL, current efficiency, and current density-voltage curves of all fabricated devices. Devices were measured in a dark sample chamber. A stylus profiler (P-6; KLA Tencor, Milpitas, CA, USA) was used to determine thickness of organic layers and an AFM (XE-150, noncontact mode; Park Systems, Suwon, Republic of Korea) was used to inspect nanostructure creation and the GTF morphology. A Protherm tube furnace (St. Louis, MO, USA) was used to anneal GTFs under different temperatures. A Varian Cary 5000 UV-Vis-NIR spectrophotometer (Palo Alto, CA, USA) was used to measure GTF UV absorbance.

Prior to depositing the GTF on the glass substrates for AFM measurement, the substrates were cleaned with detergent and then sequentially ultrasonicated for 15 min each in deionized water and isopropyl alcohol. GTFs were deposited via the physical vapor deposition technique using gold pellets on glass substrates of different thicknesses: 2.0, 4.0, 6.0, and 8.0 nm. They were annealed at 400 °C for 1 h to investigate formation of nanostructures through the AFM images. Based on the AFM images, a GTF thickness of 4.0 nm was chosen for fabricating OLEDs. The devices were prepared with a 4.0 nm GTF between ITO and HTL, and were also annealed at various temperatures to investigate temperature's effect on device performance. Device characteristics are presented in the Table. GTF-coated ITO substrates were annealed in a tube furnace for 1 h at different temperatures for each sample. All samples with a GTF were annealed from 300 °C to 600 °C with a temperature difference of 100 °C in between each sample. The fabricated devices were named according to annealing temperature, as shown in the Table. After annealing, the PEDOT:PSS layer (60 nm) was spin-coated onto the GTF at 4000 rpm for 30 s and then annealed at 110 °C for 30 min. The emissive layer (MEH-PPV; 90 nm) was spin-coated at 2000 rpm and annealed at approximately 120 °C for 10 min. The TPBi layer (40 nm) was deposited via thermal evaporation onto the emissive layer at a deposition rate of 0.1 nm/s. Finally, Ca (5 nm) and Al (120 nm) were evaporated for the cathode electrode of the devices. Ca and Al deposition rates were maintained at 0.1 nm/s and 0.3 nm/s, respectively. During thermal depositions, the chamber pressure was kept under 2×10^{-6} mbar. The thickness of the GTF, ETL, and cathode layers was controlled using a quartz-crystal monitor. The active emission area was 9.0 mm^2. The structure of the fabricated device was ITO/GTF/PEDOT:PSS/MEH-PPV/TPBi/Ca/Al, as seen in Figure 1.

Table. Properties of different the GTF thicknesses annealed at 400 °C and light-emitting characteristics of devices with a 4.0 nm GTF annealed at different temperatures.

Device name	Temperature (°C)	GTF thickness (nm)	Max. luminance (cd/m^2)	Max. current efficiency (cd/A)	AFM roughness (nm)
	400	2	-	-	4.04
	400	4	-	-	4.81
	400	6	-	-	3.08
	400	8	-	-	3.68
	No annealing	4	-	-	2.11
A0	No annealing	0 (no GTF)	1287	0.60	-
A1	300	4	40	0.31	6.18
A2	400	4	1550	0.62	4.81
A3	500	4	3286	0.66	9.40
A4	600	4	927	0.69	5.12

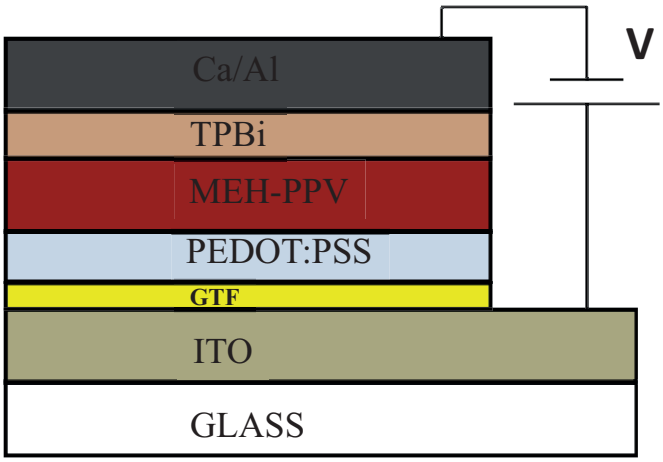

Figure 1. Schematic cross-sectional structure of the OLED used in this study.

3. Results and discussion

Effects of generated nanostructures on the device physics and performances were studied. First, structure and morphology analyses were done for different GTF thicknesses (2.0, 4.0, 6.0, and 8.0 nm) that were annealed at constant temperature (400 °C). The nanostructure sizes were changed using annealing temperatures that were well below the melting point of gold (approximately 1064 °C). Therefore, during the annealing process, there was no material loss in the GTF. Deposition rate of the gold film, stability of annealing temperature, and time after the deposition were observed in this study [44]. Maintaining a lower deposition rate (0.01 nm/s) was an important step to form nanostructures. The morphology of evaporated GTF with different thicknesses and nanostructures is shown in Figures 2a–2e. The actual size of each nanostructure was observed via AFM. Then a relationship between the nanostructure size and the GTF thickness was established according to the results. The 4.0 nm GTF without annealing (Figure 2a) was used to investigate the effect of annealing. Thermal annealing led to an increase in roughness values (Rq) due to the shape transformation, since the AFM image of a 4.0 nm GTF without annealing had an Rq of 2.11 nm. During the annealing process, the ultrathin film broke into island-like structures due to Ostwald ripening [45] and coalescence [46]. NP size (taken as the diameter of

a circle with equal area) of each sample noticeably increased as the thickness increased. As shown in Figures 2b–2d, particle sizes were about 45, 50, and 120 nm for corresponding thicknesses of 2.0, 4.0, and 6.0 nm. There was no nanostructure formation for 8.0 nm. Nanostructure sizes obtained from the 2.0 nm GTF were smaller than in the 4.0 and 6.0 nm GTFs. As the gold mass thickness increased, the island shapes became more irregular and larger. As for the size of the created nanostructures, it was interpretable as the globose structure becoming significantly amplified after annealing, probably due to the surface melting [47] of gold NPs during the annealing process [48]. As listed in the Table, Rq values were quite close to each other: 4.04, 4.81, 3.08, and 3.68 nm. Globose structures appeared on 2.0, 4.0, and 6.0 nm GTFs, but for 8.0 nm, globose structures were not clear (Figure 2d). In other words, high GTF thickness inhibited globose nanostructure formation. Gold nanostructure formation from GTF could be affected by the process of thermally deposited thin gold films on glass substrate [49]. Plasma modification of glass substrate can change the wettability of deposited gold film [48,50]. When the wettability of gold for the glass substrate was enhanced, the interactions between the two materials were stronger [50].

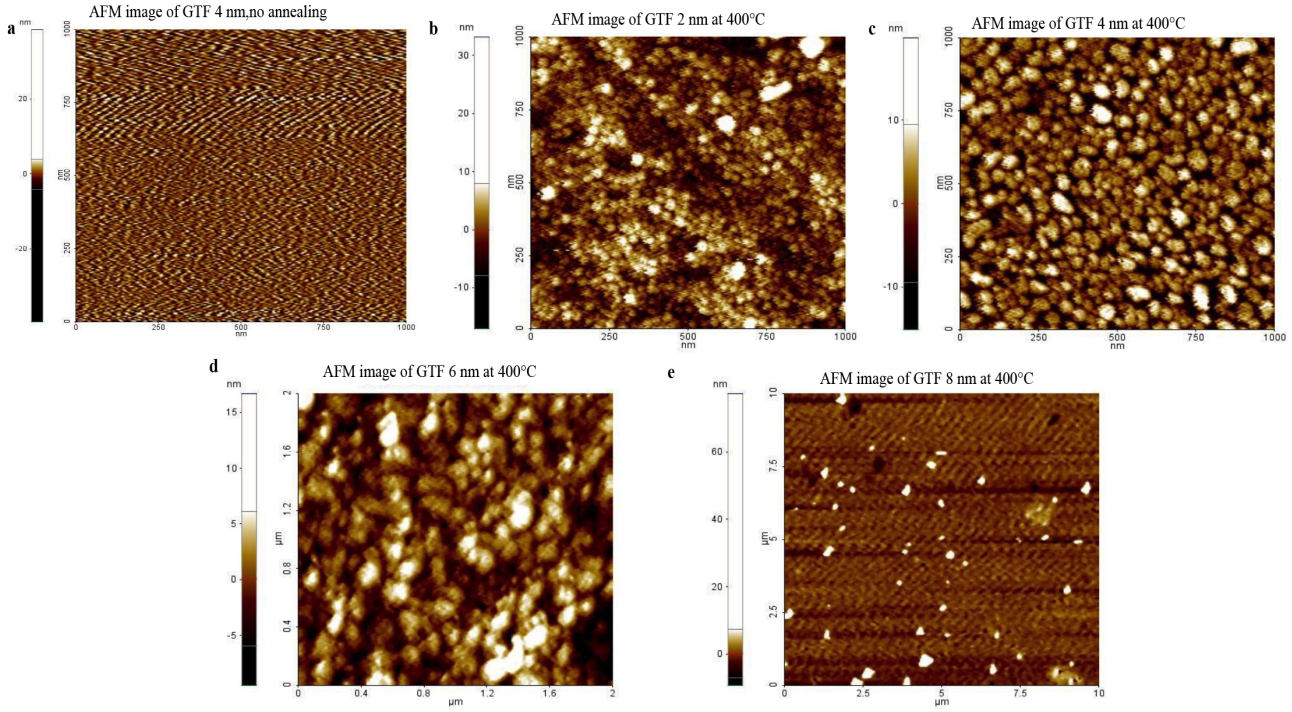

Figure 2. AFM images of GTF a) 4.0 nm, no annealing, and annealed at 400 °C with thicknesses of b) 2.0 nm, c) 4.0 nm, d) 6.0 nm, and e) 8.0 nm.

In addition, absorbance and transmittance spectra of samples with different thicknesses of GTF on glass substrates were measured in wavelengths from 400 to 800 nm. The dependence of the absorbance and transmittance spectra on the thickness of the deposited GTF was investigated. Figure 3a shows the measured absorbance spectra of the samples. There was small absorption at shorter wavelengths and an absorption dip at about 475 nm for 4.0, 6.0, and 8.0 nm. For 1.0 nm GTF, nearly no absorption could be seen, and there was a wide absorption band at wavelengths above 500 nm for other thickness values. The results showed that smaller metal particles (2.0 and 4.0 nm GTF) had low absorption in the visible region and higher absorption values above 500 nm. The absorption of the applied light onto the nanostructures deposited on the substrate

depends on each particle size. Metallic particles that are much smaller than that of the wavelength of light usually absorb more. Many researchers have studied this subject [50,51]. Therefore, in this study, there was an increase in absorption at longer (greater than 500 nm) wavelengths for larger particles (6.0 nm GTF). In Figure 3b, transmittance values can be seen; these values were inversely proportional to GTF thickness. Transmittance decreased as the GTF mass thickness increased, as expected for a metallic layer. The typical resonance peaks of gold nanostructures were present, but the absorbance was superior for the 4 nm mass thickness layer, disappearing for thicker layers.

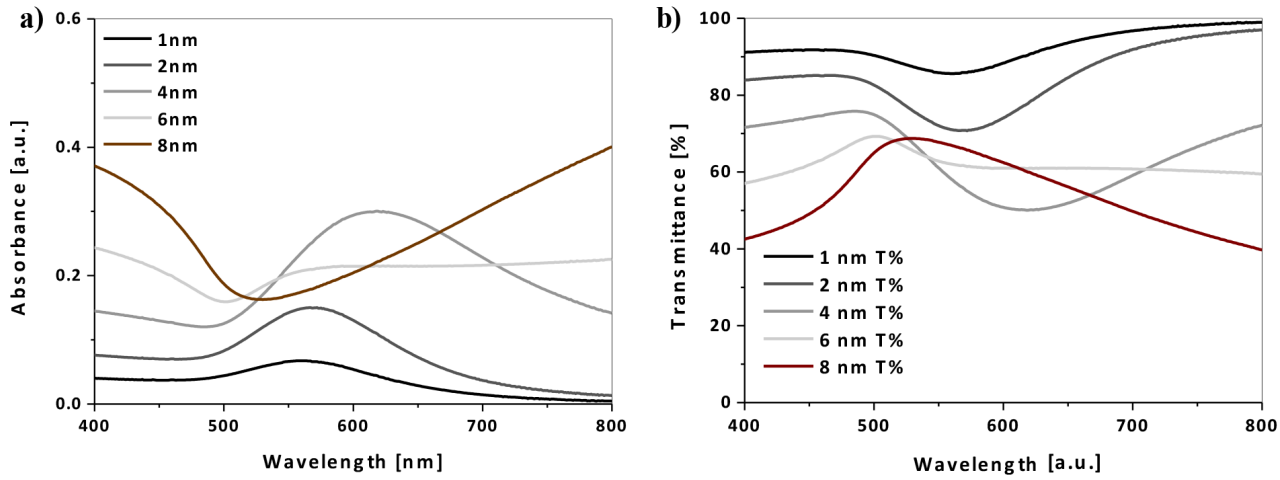

Figure 3. a) UV absorbance and b) Transmittance % spectra of 400 °C annealed GTF with different thicknesses.

The gold nanostructures obtained from the 4.0 nm GTF were utilized for device fabrication. GTFs were annealed at 300, 400, 500, and 600 °C for 1 h in a tube furnace, as presented in the Table.

Nanostructure size of each sample also noticeably increased as the annealing temperature decreased. Nanostructure sizes of 910, 50, 90, and 50 nm corresponded to annealing temperatures of 300, 400, 500, and 600 °C, respectively. As annealing temperature decreased, gold nanostructure size increased. The higher temperature a sample was annealed at, the physical property values also changed. At 300 °C, nanostructure formation was unachieved, as seen from the size of nanostructures. The GTF broke into island structures due to cooperation, and a discontinuous film transformed into regularly shaped and sized particles. Discontinuous GTFs were irregular in shape and size, and had elongated particles with large surface coverage.

Changes in the morphology and dimensions of the nanostructures, compared to other temperatures, were observed in the samples annealed at 300 °C. The rather different appearance of surface morphology was determined for evaporated GTF deposited on glass annealed at 300 °C (Figures 4a–4d). Above 300 °C, GTF started to show globose nanostructures approximately 50 nm in size, while they were approximately 910 nm for 300 °C. The description for such shape transformation could be within the formation of nanolayer and its nucleation. For this reason, the diffusion of gold nanostructures might have been annihilated when the layer was annealed, which was associated with surface wettability. In addition, surface diffusion was abolished and the nanostructure shape became regular and homogeneous during the merging process.

Figures 5a–5d show the characteristics of the OLEDs fabricated with GTF annealed at various temperatures, and the Table summarizes the measured characteristics of the devices. Device names from A0 to A4 were given according to annealing temperature: no annealing (no GTF), 300 °C, 400 °C, 500 °C, and 600 °C, respectively, as shown in the Table. A3 exhibited 3286 cd/m^2 maximum luminance (Figure 5a) and minimum

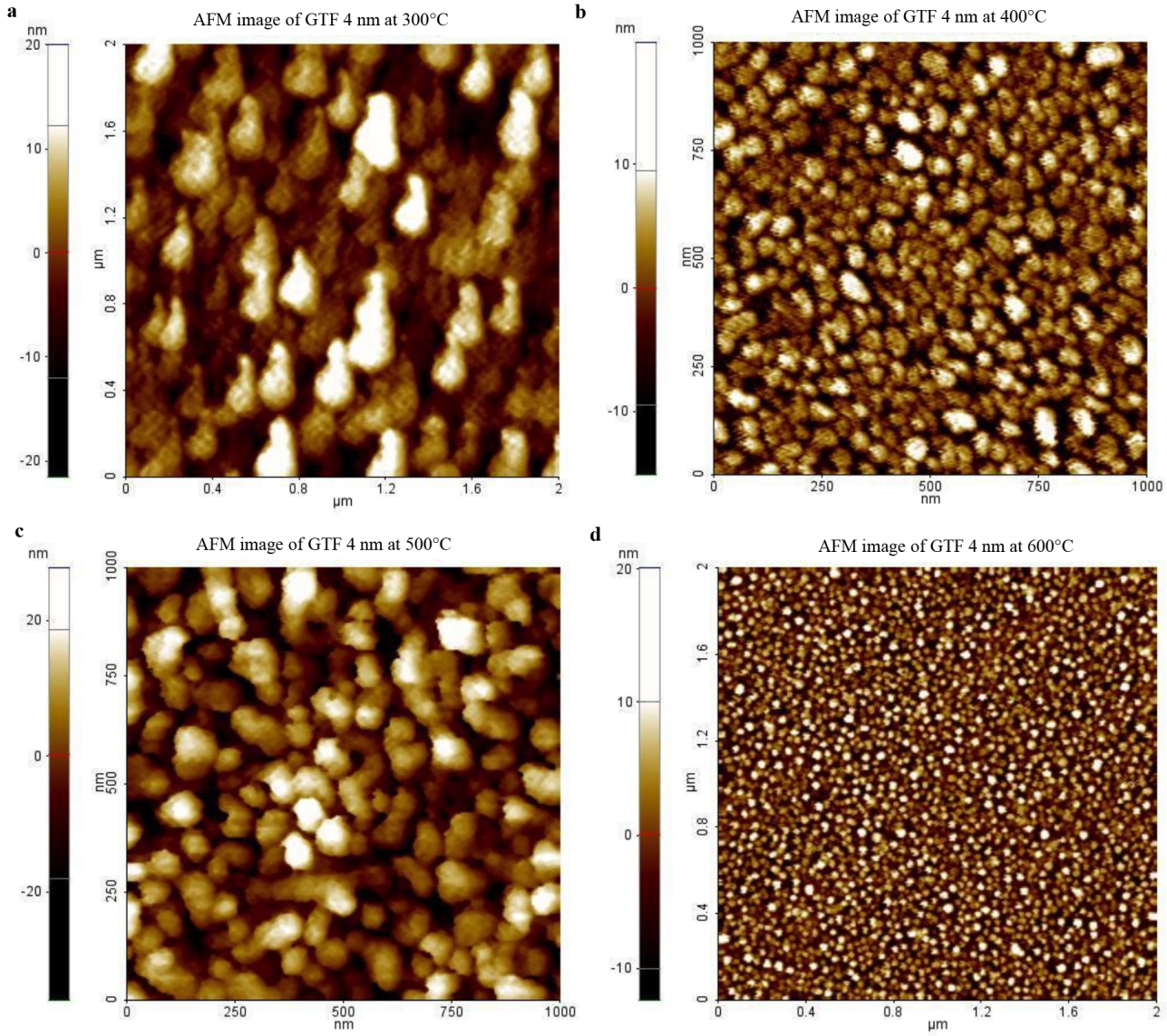

Figure 4. AFM images of 4 nm GTF annealed at a) 300 °C, b) 400 °C, c) 500 °C, and d) 600 °C.

onset voltage, 5.0 V, while the onset voltage of the device without a GTF layer was 8.0 V (Figure 5c). Here the onset voltage was the intersection of the tangent of the current density curve and the voltage axis. This is a strong indication of efficient electron injection, because GTF formed a good ohmic contact for carriers on ITO. Maximum luminance value increased more than two times upon the addition of a GTF layer annealed at 500 °C, while it was 426.1 cd/m^2 for A0. Furthermore, the onset voltages were nearly the same for A0, A1, A2, and A4. The optimized annealing temperature was 500 °C, which gives the highest luminance and the lowest onset voltage with respect to the other annealing temperatures. The current efficiencies of the devices nearly had the same value, except A1. A1 had the lowest luminance (40.4 cd/m^2); since current density of the device A1 was the lowest, its current efficiency was also the lowest. As mentioned above, for the device A1, the size of nanostructures was 910 nm at an annealing temperature of 300 °C. It is possible that Schottky barriers that formed between contacts became dominant and electron transport was delayed in the conduction bands for the

bigger nanostructures. In Figure 5d, normalized EL intensity characteristics can be seen. From the spectra, the emissions of 600 °C, 500 °C, 400 °C, and no GNP were almost the same in shape and peak wavelength values (597 nm). This was consistent with the MEH-PPV emission profile. However, 300 °C showed different EL characteristics from the others. There were two main peaks at 598 and 642 nm. The first peak had the same characteristics but lower intensity than the other temperatures. The second main peak was at the red emission wavelength. This could be attributed to the 910 nm nanostructure formation. NP formation was unachieved and the film broke into island structures. This could cause the charge traps with lower energy levels in the interface of the device. The charge carriers could choose low-energy ways to recombine each other.

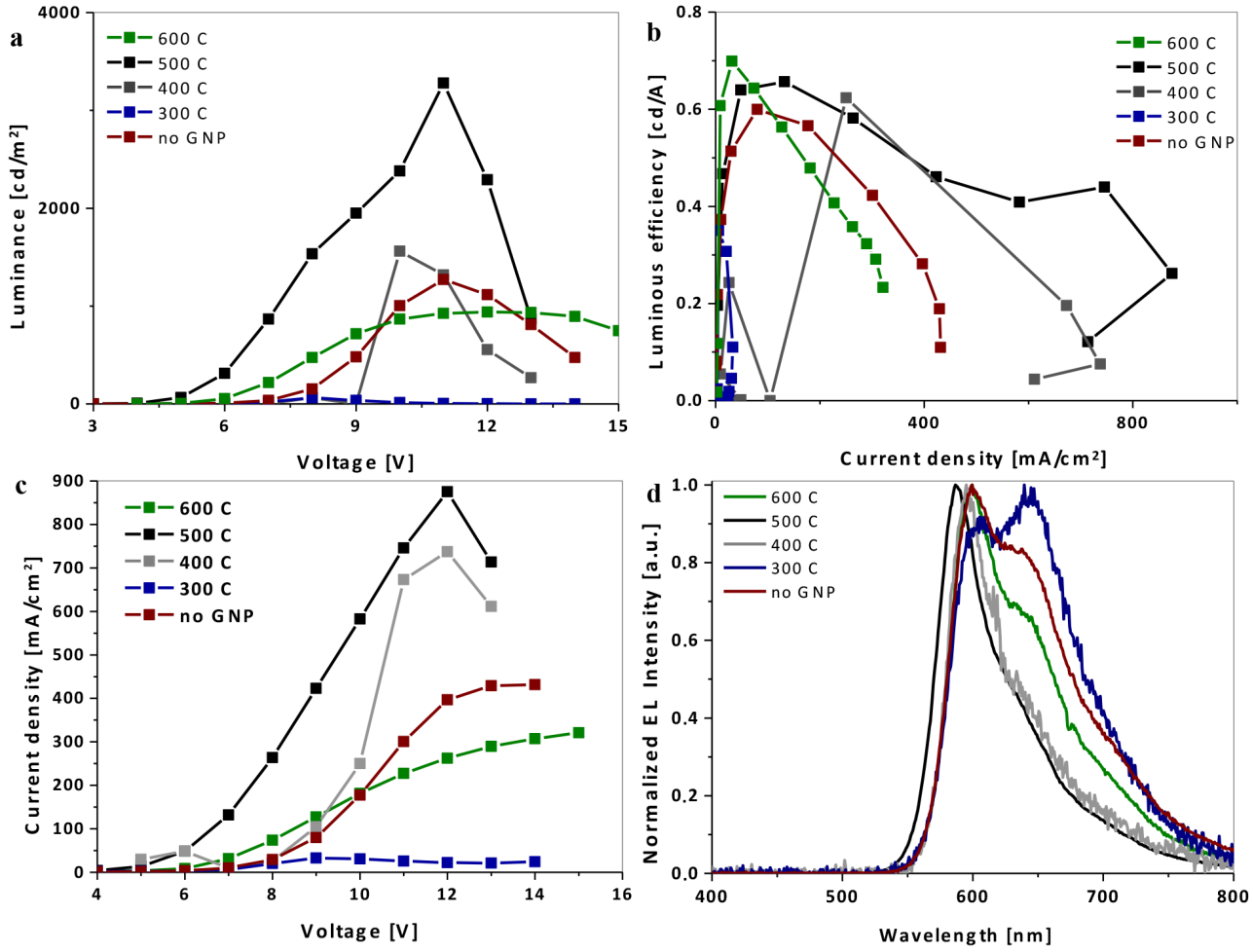

Figure 5. a) Luminance-voltage, b) luminous efficiency-current density, c) current density-voltage, d) normalized EL intensity characteristics of OLEDs fabricated with a 4 nm GTF annealed at 300 °C, 400 °C, 500 °C, and 600 °C.

An energy diagram of the materials is presented in Figure 6. Gold energy level was appropriate for ITO and HTL. Therefore, easier transport could be provided for holes coming from ITO. This means that more efficient recombination between electrons and holes in the emissive layer was established. As clearly seen in Figure 6, the lowest TPBi unoccupied molecular orbital (LUMO) energy level matched the LUMO energy level of the emissive layer, and thus the transportation of electrons from cathode to emissive layer becomes easier. In other words, ETL lowered the potential energy barrier for electrons. TPBi also had the highest occupied molecular orbital energy level, which was high enough to block the transportation of holes to the cathode. Small

TPBi molecules have been used both as a host material and as an electron transport material for OLEDs based on fluorescent and phosphorescent emitters [52–55]. TPBi has a low electron affinity (2.7 eV) and a higher

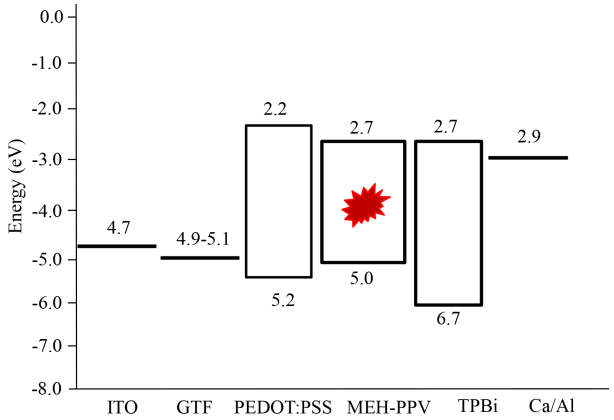

Figure 6. The energy diagram for OLED. The highest occupied molecular orbital and lowest unoccupied molecular orbital band energies.

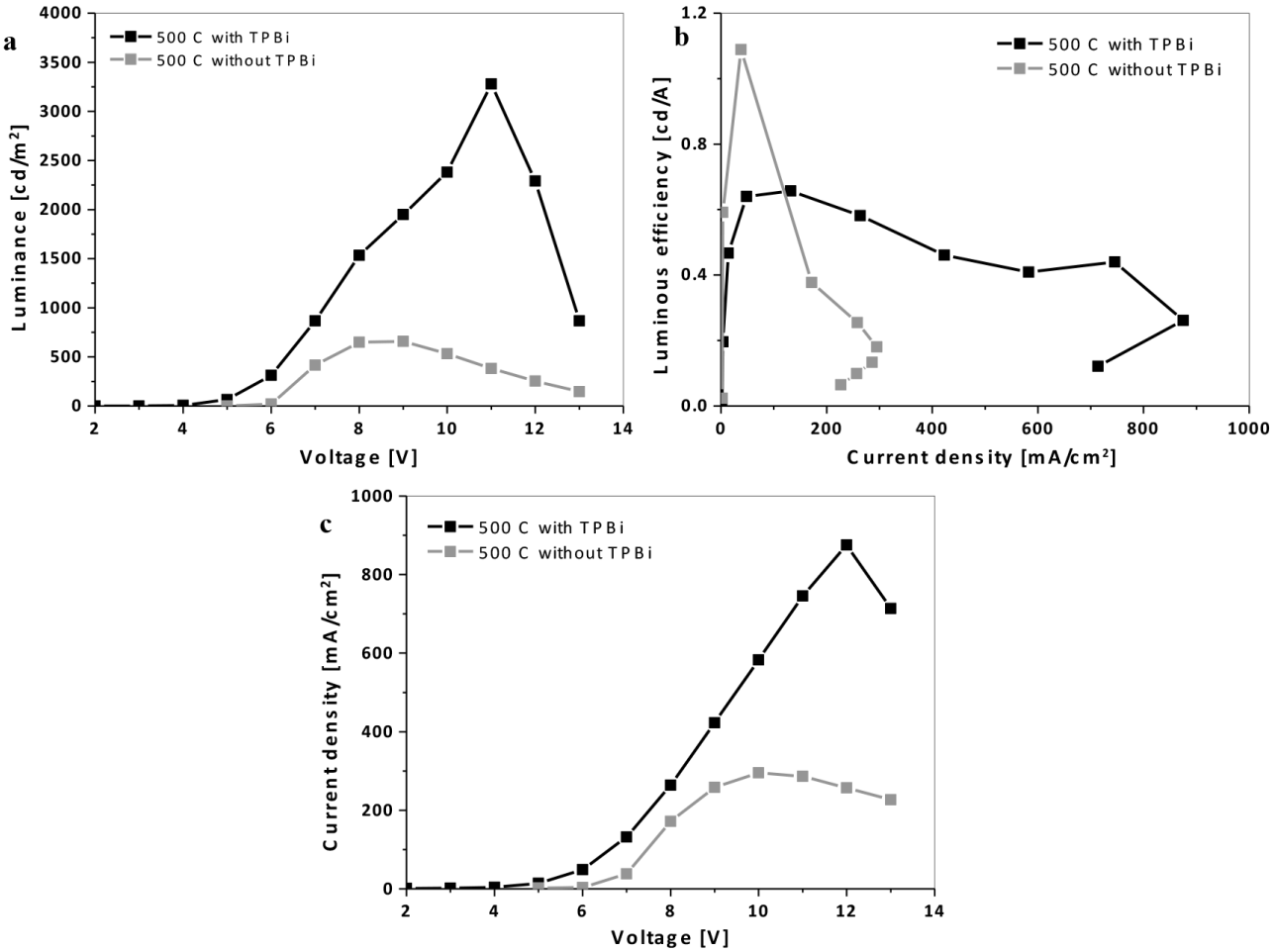

Figure 7. a) Luminance-voltage, b) luminous efficiency-current density, c) current density-voltage characteristics of OLEDs with a 4.0 nm GTF annealed at 500 °C and fabricated with/without TPBi.

ionization potential (6.2–6.7 eV) [56]. This study surveyed enhancement in optical and electrical mechanisms, such as luminance, luminous efficiency, and current-voltage characteristic, when using TPBi for OLEDs. A TPBi layer was chosen not only because it is a good electron-transporting layer and hole-blocking layer (in other words, it provides carrier balance in the device), but also because it emits almost no EL, which guarantees the color purity of the EL spectra. The ETL provided facile charge (electron) transport to the emissive layer, because the TPBi has high electron mobility. Thus, lower current densities were obtained when using a TPBi compared to devices without this ETL. TPBi improved the blocking characteristics of abundant holes, which reduced the leakage current. As a result, this improved luminance efficiency via efficient recombination of electrons and holes in the emissive layer. Figure 7 illustrates device characteristics with/without a TPBi layer. There was a six-fold enhancement in luminance and a nearly two-fold enhancement in current efficiency when comparing devices with and without a TPBi layer.

4. Conclusion

The optical and the physical properties of gold nanostructures grown on a glass substrate were investigated. GTFs of various thicknesses, deposited via thermal evaporation, were used for the creation of nanostructures via thermal annealing at different temperatures. Then, due to surface tension, the gold nanostructures merged together to form islands. This process was one of the practical ways to deposit metal nanostructures onto a substrate. At a thickness of 8.0 nm, nanostructures were not observed, because separation into nanoislands was not possible at 400 °C. Absorption also changed as the particles grew due to the different thickness of the film. According to AFM roughness data, the optimum thickness was 4.0 nm. Thermal annealing was applied at different temperatures for OLED fabrication. Nanostructure size on each sample changed in each different case. As the temperature decreased, the gold nanostructures grew larger in size and geometry. The device with a 4.0 nm GTF annealed at 500 °C exhibited 3286 cd/m^2 maximum luminance and minimum onset voltage, 5.0 V. Maximum luminance increased more than 2.6 times upon addition of a GTF layer annealed at 500 °C, while it was 1290 cd/m^2 for the device without a GTF.

This work has shown that gold nanostructures created by thermal annealing can be different in their physical and optical properties. Modification of these nanostructures can improve OLED efficiency.

References

[1] Bradley, D. D. C. *Adv. Mater.* **1992**, *4*, 756-758.

[2] Meng, Z. L. H. *Organic Light-Emitting Materials and Devices*; CRC Press: Boca Raton, FL, USA, 2007.

[3] Hide, F.; Dias-Garcia, M. A.; Schwartz, B. J.; Heeger, A. J. *Acc. Chem. Res.* **1997**, *30*, 430-436.

[4] Crone, B.; Dodabalapur, A.; Lin, Y.Y.; Filas, R. W.; Bao, Z.; LaDuca, A.; Sarpeshkar, R.; Katz, H. E.; Li, W. *Nature* **2000**, *403*, 521-523.

[5] PıravadılıMucur, S.; Tumay, T. A.; Birdoğan, S.; San, S. E.; Tekin, E. *Nano Structures and Nano Objects* **2015**, *1*, 7-14.

[6] PıravadılıMucur, S.; Duygulu, Ö.; San, S. E.; Tekin, E.; Denizci, A.; Utkan, G.; Öztürk, H. Ü. *Opt. Mat.* **2015**, *47*, 297-303.

[7] PıravadılıMucur, S.; San, S. E.; Tekin, E.; Holder, E.; Lenkeit, D.; Kanelidis, I. *J. Polym. Sci. Part B: Polym. Phys.* **2014**, *52*, 147-156.

[8] PıravadılıMucur, S.; San, S. E.; Tekin, E.; Tumay, T. A. *J. Nanopart. Res.* **2012**, *14*, 1214-1223.

[9] Xu, K.; Li, Y.; Zhang, W.; Zhang, L.; Xie, W. *Curr. App. Phys.* **2014**, *14*, 53-56.

[10] Salata, O. V. *J. Nanobiotechnol.* **2004**, *2*, 3-9.

[11] Lee, K.; El-sayed, M. A. *J. Phys. Chem. B* **2006**, *110*, 19220-19225.

[12] Matsui, I. *J. Chem. Eng. Jpn.* **2005**, *38*, 535-546.

[13] Chen, W.; Zhang, J. Z.; Joly, A. G. *J. Nanosci. Nanotechnol.* **2004**, *4*, 8.

[14] Soppimath, K. S.; Aminabhavi, T. M.; Kulkarni, A. R.; Rudinski W. E. *J. Control. Rel.* **2001**, *70*, 1-20.

[15] Govorov, A. O.; Richardson, H. H. *Nanotoday* **2007**, *2*, 30-38.

[16] Liu, F.; Aldea, G.; Nunzi, J. M. *J. Lumin.* **2010**, *130*, 56-59.

[17] Nie, S.; Emory, S. R. *Science* **1997**, *275*, 1102-1106.

[18] Parlak, E. A.; Tumay, A.; Tore, N.; Sarıoğlan, Ş.; Kavak, P.; Türksoy, F. *Sol. Energy Mater. Sol. Cells* **2013**, *110*, 58-62.

[19] Westphalen, M.; Kreibig, U.; Rostalski, J.; Luth, H.; Meissner, D. *Sol. Energy Mater. Sol. Cells* **2000**, *61*, 97-105.

[20] Wang, Z.; Chumanov, J. *Adv. Mater.* **2003**, *15*, 1285-1289.

[21] Nah, Y. C.; Kim, S. S.; Park, J. H.; Kim, D. Y. *Electrochem. Solid-State Lett.* **2007**, *10*, 12-14.

[22] Okamoto, K.; Niki, I.; Shvartser, A.; Narukawa, Y.; Mukai, T.; Scherer, A. *Nat. Mater.* **2004**, *3*, 9-15.

[23] Yates, C. J.; Samuel, I. D. W.; Burn, P. L.; Wedge, S.; Barnes, W. L. *Appl. Phys. Lett.* **2006**, *88*, 161105.

[24] Pillai, S.; Catchpole, K. R.; Trupke, T.; Zhang, G.; Zhao, J.; Green, M. A. *Appl. Phys. Lett.* **2006**, *88*, 161102.

[25] Jain, P. K.; El-Sayed, I. H.; El-Sayed, M. A. *Nanotoday* **2007**, *2*, 1.

[26] Govorov, O.; Zhang, W.; Skeini, T.; Richardson, H.; Lee, J.; Kotov, A. *Nanoscale Res. Lett.* **2006**, *1*, 84-90.

[27] Wang, Z. J.; Zhang, J.; Yin, Z. Y.; Wu, S. X.; Mandler, D.; Zhang, H. *Nanoscale* **2012**, *4*, 2728-2733.

[28] Schedin, F.; Geim, A. K.; Morozov, S. V.; Hill, E. W.; Blake, P.; Katsnelson, M. I. *Nat. Mater.* **2007**, *6*, 652-655.

[29] Johnson, J. L.; Behnam, A.; Pearton, S. J.; Ural, A. *Adv Mater.* **2010**, *22*, 4877-4880.

[30] Xiao, Y.; Yang, J. P.; Cheng, P. P.; Zhu, J. J.; Xu, Z. Q.; Deng, Y. H.; Lee, S. T.; Li, Y. Q.; Tang, J. X. *Appl. Phys. Lett.* **2012**, *100*, 013308.

[31] Kumar, A.; Srivastava, R.; Tyagi, P.; Mehta, D. S.; Kamalasanan, M. N. *Org. Electr.* **2012**, *13*, 1623-1632.

[32] Kealley, C. S.; Cortie, M. B.; Maaruf, A. I.; Xu, X. *Phys Chem Chem Phys.* **2009**, *11*, 5897-5902.

[33] Xu, X.; Stevens, M.; Cortie, M. B. *Chem. Mater.* **2004**, *16*, 2259-2266.

[34] Xu, X.; Cortie, M. B.; Stevens, M. *Mater. Chem. Phys.* **2005**, *94*, 266-274.

[35] Zhou, H.; Yu, F.; Chen, M.; Qiu, C.; Yang, H.; Wang, G.; Yu, T.; Sun, L. *Carbon* **2013**, *52*, 379-387.

[36] Hardy, N. J.; Richardson, T. H. *Colloids Surf., A: Physicochem. Eng. Aspects* **2008**, *321*, 285-291.

[37] Ung, T.; Liz-Marzan, L. M.; Mulvaney, P. *Colloids Surf., A: Physicochem. Eng. Aspects* **2002**, *202*, 119-126.

[38] Schaub, A.; Slepicka, P.; Kašpárková, I.; Malinsky, P.; Macková, A.; Švorcík, V. *Nanoscale Res. Lett.* **2013**, *8*, 249-257.

[39] Romani, E. C.; Vitoreti, D.; Gouvêa, P. M. P.; Caldas, P. G.; Paciornik, S.; Fokine, M.; Braga, A. M. B.; Gomes, A. S. L.; Prioli, R.; Carvalho, I. C. S. *Opt. Express* **2012**, *20*, 5429-5439.

[40] Ahamad, N. U.; Al-Amin, M.; Ianoul, A. *J. Nanopart. Res.* **2014**, *2014*, 1-9.

[41] Ahn, W.; Taylor, B.; Dall'Asen, A. G.; Roper, D. K. *Langmuir* **2008**, *24*, 4174-4184.

[42] Kruisa, F. E.; Fissana, H.; Peled, A. *J. Aerosol Sci.* **1998**, *29*, 511-535.

[43] Kılıç, B.; Gür, E.; Gedik, N.; PıravadılıMucur, S.; Hergul, A. S. *Mater. Sci. Semicond. Process.* **2015**, *31*, 363-371.

[44] Hopfner, U.; Hehl, H.; Brehmer, L. *Appl. Surf. Sci.* **1999**, *152*, 259-265.

[45] Yao, J. H.; Elder, K. R.; Guo, H.; Grant, M. *Phys. Rev. B* **1993**, *47*, 14110-14125.

[46] Arcidiacono, S.; Bieri, N. R.; Poulikakos D.; Grigoropoulos C. P. *Int. J. Multiphas. Flow* **2004**, *30*, 979-994.

[47] Müller, P.; Kern, R. *Surf. Sci.* **2003**, *529*, 294-296.

[48] Švorčík, V.; Siegel, J.; Šutta, P.; Mistrík, J.; Janíček, P.; Worsch, P.; Kolská, Z. *Appl. Phys. A* **2011**, 102, 3.

[49] Roland, T.; Khalil, A.; Tanenbaum, A.; Berguiga, L.; Delichère, P.; Bonneviot, L.; Elezgaray, J.; Arneodo, A.; Argoul, F. *Surf. Sci.* **2009**, *603*, 3307-3320.

[50] Pillai, S.; Catchpole, K. R.; Trupke, T.; Green, M. A. *J. Appl. Phys.* **2007**, *101*, 093105.

[51] Gaspar, D.; Pimentel, A. C.; Mateus, T.; Leitão, J. P.; Soares, J.; Falcão, B. P.; Araújo, A.; Vicente, A.; Filonovich, S. A.; Águas, H.; et al. *Sci. Reports* **2013**, *3*, 1469.

[52] Duan, J. P.; Sun, P. P.; Cheng, C. H. *Adv. Mater.* **2003**, *15*, 224.

[53] Thomas, J. K. R.; Lin, J. T.; Tao, Y. T.; Chuen, C. H. *Chem. Mater.* **2002**, *14*, 3852.

[54] Shih, H. T.; Lin, C. H.; Shih, H. H; Cheng, C. H. *Adv. Mater.* **2002**, *14*, 1409.

[55] Gao, Z.; Lee, C. S.; Bello, I.; Lee, S. T.; Chen, R. M.; Luh, T. Y; Shi, J.; Tang, C. W. *Appl. Phys. Lett.* **1999**, *74*, 865.

[56] Shih, H. T.; Lin, C. H.; Shih, H. H.; Cheng, C. H. *Adv. Mater.* **2002**, *14*, 1409-1412.